Research
A SCIENCE PARTNER JOURNAL

RESEARCH ARTICLE

Unimolecular Reactions of *E*-Glycolaldehyde Oxide and Its Reactions with One and Two Water Molecules

Yan Sun[1], Bo Long[1,2*], and Donald G. Truhlar[3*]

[1]Department of Physics, Guizhou University, Guiyang 550025, China. [2]College of Materials Science and Engineering, Guizhou Minzu University, Guiyang 550025, China. [3]Department of Chemistry, Chemical Theory Center, and Supercomputing Institute, University of Minnesota, Minneapolis, MN 55455-0431, USA.

*Address correspondence to: wwwltcommon@sina.com (B.L.); truhlar@umn.edu (D.G.T.)

Citation: Sun Y, Long B, Truhlar DG. Unimolecular Reactions of *E*-Glycolaldehyde Oxide and Its Reactions with One and Two Water Molecules. *Research* 2023;6:Article 0143. https://doi.org/10.34133/research.0143

Submitted 5 January 2023
Accepted 20 April 2023
Published 10 July 2023

Copyright © 2023 Yan Sun et al. Exclusive licensee Science and Technology Review Publishing House. No claim to original U.S. Government Works. Distributed under a Creative Commons Attribution License 4.0 (CC BY 4.0).

The kinetics of Criegee intermediates are important for atmospheric modeling. However, the quantitative kinetics of Criegee intermediates are still very limited, especially for those with hydroxy groups. Here, we calculate rate constants for the unimolecular reaction of *E*-glycolaldehyde oxide [*E*-hydroxyethanal oxide, *E*-(CH_2OH)CHOO], for its reactions with H_2O and $(H_2O)_2$, and for the reaction of the *E*-(CH_2OH)CHOO...H_2O complex with H_2O. For the highest level of electronic structure, we use W3X-L//CCSD(T)-F12a/cc-pVDZ-F12 for the unimolecular reaction and the reaction with water and W3X-L//DF-CCSD(T)-F12b/jun-cc-pVDZ for the reaction with 2 water molecules. For the dynamics, we use a dual-level strategy that combines conventional transition state theory with the highest level of electronic structure and multistructural canonical variational transition state theory with small-curvature tunneling with a validated density functional for the electronic structure. This dynamical treatment includes high-frequency anharmonicity, torsional anharmonicity, recrossing effects, and tunneling. We find that the unimolecular reaction of *E*-(CH_2OH)CHOO depends on both temperature and pressure. The calculated results show that *E*-(CH_2OH)CHOO...H_2O + H_2O is the dominant entrance channel, while previous investigations only considered Criegee intermediates + $(H_2O)_2$. In addition, we find that the atmospheric lifetime of *E*-(CH_2OH)CHOO with respect to 2 water molecules is particularly short with a value of 1.71×10^{-6} s at 0 km, which is about 2 orders of magnitude shorter than those usually assumed for Criegee intermediate reactions with water dimer. We also find that the OH group in *E*-(CH_2OH)CHOO enhances its reactivity.

Introduction

Criegee intermediates [1] are key atmospheric species derived from the ozonolysis of volatile unsaturated organic compounds in the atmosphere [2–4]. Their unimolecular reactions are often considered to be the main nonphotolytic source of the OH cleanser radical during the night [4–14], although atmospheric OH formation from photolytic sources significantly exceeds that from ozonolysis in general. Criegee intermediates also make important contributions as sinks for other atmospheric species [3,15–22], and they significantly influence the budget of sulfuric acid [19,23–28], the growth of secondary organic aerosols [29–34], and the production of some highly oxygenated products [35–38]. The rate constants of Criegee intermediates are key parameters for elucidating these chemical transformations; however, experimental knowledge of these rate constants is limited [39–41].

C5-C6 unsaturated alcohols such as *Z*-2-penten-1-ol and *E*-2-hexen-1-ol [42–47] have been found to be widespread in the atmosphere [42,48–53]. The atmospheric sink of these unsaturated alcohols is ozonolysis [42,46,54,55], and ozonolysis reactions can produce *E*-CH_2(OH)CHOO (i.e., *E*-hydroxyethanal oxide, also known as *trans*-glycolaldehyde oxide or *anti*-glycolaldehyde oxide, where the hydroxymethyl group is *trans* to the oxide oxygen, as shown in Fig. 1) and *Z*-CH_2(OH)CHOO [where the terminal oxygen atom is *cis* (also called *syn*) to CH_2OH][43]. The

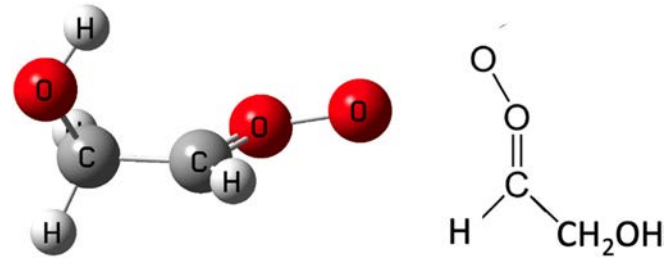
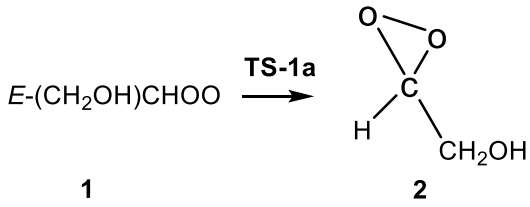


Fig. 1. Two representations of *E*-glycolaldehyde oxide.

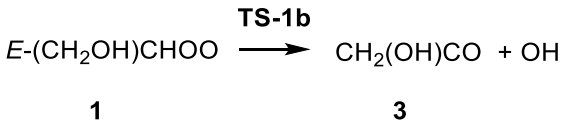
conversion between them requires high activation enthalpy (~40 kcal/mol at 0 K), which means they are not in equilibrium and react independently [56–58]. The relative yield of the two isomers depends on the starting alkene [58–61]. The present article focuses on the *trans* isomer.

Investigation of *E*-CH_2(OH)CHOO kinetics has been carried out theoretically but not experimentally. There is one theoretical study, which is due to Vereecken et al. [62] who investigated the unimolecular reaction of *E*-CH_2(OH)CHOO and its bimolecular reaction with H_2O by using CCSD(T)//M06-2X with a beyond CCSD(T) empirical correction based on a large amount of data. Because obtaining quantitative kinetics by theoretical methods requires reliable geometrical optimizations, zero-point vibrational energies, and single-point energies [63], further theoretical calculations are required to check those results.

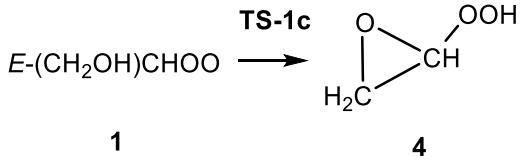
The present article is concerned with obtaining quantitative kinetics of the unimolecular reaction of *E*-CH_2(OH)CHOO and the reaction of this intermediate with atmospheric water vapor by using theoretical methods. We chose *E*-CH_2(OH)CHOO as a prototype to understand the effects of hydroxy substituents on Criegee intermediates. We consider only reactions of stabilized Criegee intermediates, and we caution that nascent Criegee intermediates may show different reactivity. The reactions considered are as follows:



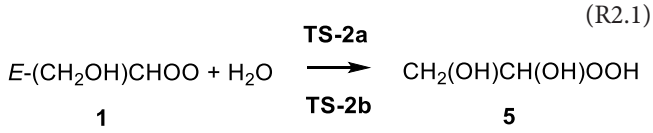
(R1a)



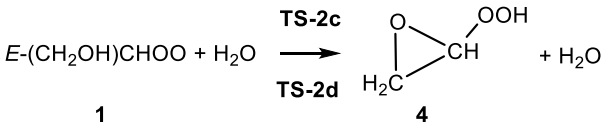
(R1b)



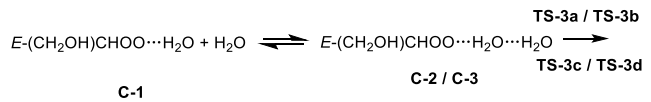
(R1c)



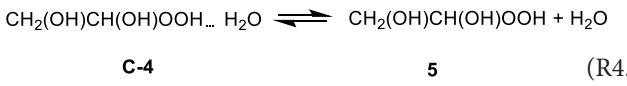
(R2.1)



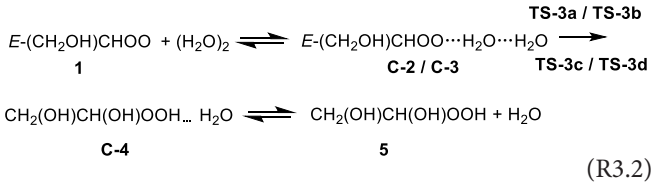
(R2.2)



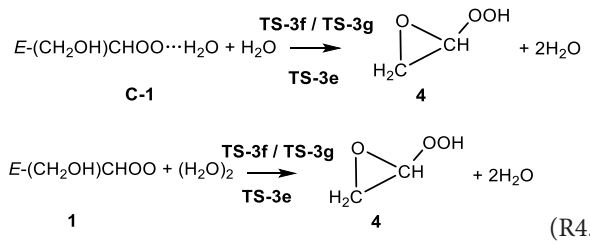
(R3.1)



(R4.1)



(R3.2)



(R4.2)

Water vapor is studied as a reactant because there are high concentrations of water monomers (~10^{17} molecules cm^{-3}) [64,65] and water dimers (~10^{14} molecules cm^{-3}) [56,66] in the troposphere. Moreover, previous investigations have shown that water vapor is a dominant sink for the simplest Criegee intermediate (CH_2OO) [56,62,66–69].

Computational Methods

Dynamics: Methods

The rate constant calculations in the present paper were carried out by variational transition state theory (VTST) [70,71]. In the present work, we write the VTST rate constant as a product of factors.

The first factor equals the one-way equilibrium flux of reactants through a hypersurface in phase space dividing reactants from products [72–75]. The hypersurface is called the dividing surface or the transition state. When the dividing surface runs through a first-order saddle point and is normal to the imaginary-frequency normal mode, it is called the conventional transition state, and the first factor is called the conventional transition state theory rate constant. When applied to a unimolecular reaction, it is sometimes called Rice–Ramsperger–Kassel–Marcus (RRKM [76]) theory. Note that the transition state is missing one degree of freedom, which is the degree of freedom normal to the dividing surface and which is called the reaction coordinate. This first factor can be written as [77,78]

$$k_{\mathrm{TST}} = \frac{k_B T}{hC^0} \exp\left[-\frac{\Delta G_T^{\mathrm{TS},0}}{RT}\right] \quad (1)$$

where k_B, h, T, and R are the Boltzmann constant, Planck constant, temperature, and gas constant, respectively; C^0 is the reciprocal of the standard-state concentration for bimolecular reactions and unity for unimolecular reactions; and $\Delta G_T^{\mathrm{TS},0}$ is the conventional transition state theory standard-state free energy of activation defined by

$$\Delta G_T^{\mathrm{TS},0} = G_T^{\mathrm{TS},0} - G_T^{\mathrm{R},0} \quad (2)$$

where $G_T^{\mathrm{TS},0}$ is the standard-state Gibbs free energy of the conventional transition state and $G_T^{R,0}$ is the standard-state Gibbs

free energy of reactants (the subscript T is the temperature). Because the conventional transition state is not a stable species, Eq. 2 is a quasithermodynamic formulation. In general, the flux through the dividing surface can be calculated by classical trajectories [79–81] or by making the harmonic or quasiharmonic approximation and using the partition functions of statistical mechanics. Because the reactants are assumed to be in local equilibrium, transition state theory is sometimes called a statistical theory, but that should not obscure the fact that it is the calculation of a dynamical flux. An advantage of the partition function formulation is that one may use quantum mechanical partition functions; this replaces the classical calculation of the flux through the dividing surface by a quantized one, which is sometimes called quasiclassical. Since the transition state is missing one degree of freedom, the quasiclassical formulation quantizes all degrees of freedom except the reaction coordinate. In the present work, we use the quasiclassical partition function method with the quasiharmonic approximation.

The quasiharmonic approximation consists of using the harmonic oscillator formulas for the vibrational partition functions, but with scaled vibrational frequencies that account for anharmonicity in small-amplitude vibrations and for systematic errors in the method used to calculate vibrational frequencies. When the reacting system has multiple conformations (multiple structures), the anharmonicity of torsional vibrations can be accounted for by multiplying by the multistructural torsion (MS-T) factor F_{act}, which equals the ratio of the multistructural rate constant [82] to the single-structural rate constant.

The final factor in the rate constant calculations is called the transmission coefficient. It may be written as a product of 3 more factors:

$$\gamma = \Gamma\kappa g$$

where Γ is the recrossing transmission coefficient, κ is the tunneling transmission coefficient, and g accounts for nonequilibrated reactants.

The recrossing transmission coefficient is defined as the ratio of the single-structure VTST rate constant to the single-structure conventional transition state theory rate constant. VTST again involves the flux though a surface, but the surface is chosen variationally to minimize the flux so that the one-way flux is a closer approximation to the net flux; minimizing the flux is equivalent to minimizing recrossing [70].

The tunneling transmission coefficient is the ratio of the dynamical flux calculated with tunneling and nonclassical reflection to that calculated quasiclassically. When the tunneling is calculated with a one-dimensional model, this may be considered the effect of adding quantum effects to the reaction coordinate. In our work, we use the small-curvature tunneling approximation [83], which is a multidimensional tunneling calculation that also includes nonseparable coupling of the reaction coordinate to the other degrees of freedom.

The nonequilibrium factor g is approximated as unity for bimolecular reactions, where the rate constant is assumed to be independent of pressure, and for the high-pressure limit (HPL) of unimolecular reactions. The final VTST rate constant for these cases is

$$k_{HPL} = F_{act}\,\Gamma\kappa k_{TST} \tag{3}$$

where k_{TST} is the single-structure, quasiclassical, quasiharmonic conventional transition state theory rate constant.

For finite-pressure unimolecular reactions, one must consider the competition between depletion of energized states of the reactant due to reaction and pressure-dependent repopulation of those states by energy transfer collisions. We calculated the pressure dependence of the isomerization reaction R1a in 2 ways: system-specific quantum Rice–Ramsperger–Kassel (SS-QRRK) theory [84,85] and a master equation treatment.

Dynamics: Levels

For R1a and R2.1, dual-level [56,57,66,86–92] multistructural [82] canonical VTST [70] with small-curvature tunneling [83] (DL-MS-CVT/SCT) [93] was used to obtain high-pressure-limit rate constants $\left(k_{HPL}^{DL}\right)$ by the following equation:

$$k_{HPL}^{DL} = \frac{k_{TST}^{SS-HL}}{k_{TST}^{SS-LL}}\, k_{MS-CVT/SCT}^{LL} = F_{act}\,\Gamma\kappa\, k_{TST}^{SS-HL} \tag{4}$$

where k_{TST}^{SS-HL} and k_{TST}^{SS-LL} denote higher-level and lower-level conventional transition state theory, respectively, employing the lowest-energy conformers of the reactants and transition states; κ is a tunneling transmission coefficient calculated by the small-curvature tunneling approximation for the lowest-energy reaction path; Γ is a recrossing transmission coefficient $\left(k_{CVT}^{SS-LL}/k_{TST}^{SS-LL}\right)$, calculated by canonical variation transition state theory for the lowest-energy reaction path; and F_{act} is the multistructural anharmonicity factor calculated by MS-T(coupled) [94]. All these calculations except k_{TST}^{SS-HL} are based on the lower level of electronic structure.

For R3.1 and R4.1, the rate-determining step at low temperatures is from the reactant to the pre-reaction complex. Therefore, for R3.1 and R4.1, we used the deep-intermediate limit [66] of canonical unified statistical theory (CUS) [95,96]

$$k_x = \frac{k_x' k_x''}{k_x' + k_x''} \tag{5}$$

where k_x'' is calculated for the association reaction as calculated by variable reaction coordinate variational transition-state theory [97,98] and k_x' is the rate constant for passing through the tight transition state (**TS-3a**, **TS-3b**, **TS-3c**, and **TS-3d**) as calculated by DL-MS-CVT/SCT) using Eq. 4. The rate constant k_x'' is for **C-1** + H_2O → **C-2**/**C-3** for R3.1 and is for **1**+$(H_2O)_2$ → **C-2**/**C-3** for R4.1. The rate constant k_x' is for **C-1** + H_2O → **5** + H_2O for R3.1 and is for **1** + $(H_2O)_2$ → **5** + H_2O for R4.1. We use CUS only in the HPL.

We explored the pressure dependence of the isomerization reaction R1a in 2 ways. (a) We used SS-QRRK theory with DL-MS-CVT/SCT rate constants as input. (b) We used the master equation with RRKM rate constants as input.

Dynamics: Software

Polyrate 2017C and Gaussrate 2017B [99] were carried out to obtain k_{TST}^{SS-LL}, k_{TST}^{SS-HL}, Γ, and κ. In addition, MESS [100] and Polyrate 2017C were used for pressure dependence calculations. The torsional anharmonicity calculation and conformation search were performed using MSTor [101,102].

Electronic structure: Acronyms and abbreviations

To make the paper easier to read and the notation less cumbersome, we use standard acronyms for electronic structure

methods and basis sets. These are explained with references in Table 1.

All enthalpies of activation in this article are calculated by conventional transition state theory without tunneling and are for a temperature of 0 K. These values should not be confused with phenomenological enthalpies of activation calculated from observable rate constants because the phenomenological ones contain contributions from variational effects, recrossing, tunneling, and nonequilibrium effects [78].

Anharmonicity

To treat anharmonicity and correct for systematic errors in calculated frequencies, we included anharmonicity by 2 methods: frequency scaling and torsional anharmonicity.

Scaling factors account for anharmonicity of small-amplitude vibrations and for systematic errors in specific combinations of density functional and basis sets [103]. Previous work has shown that these scale factors are largely transferable for calculating zero-point energies of stable species (the zero-point energy is dominated by small-amplitude, high-frequency vibrations), but sometimes they are quite significantly different for transition states and low-frequency vibrations. Two parametrizations are considered here: generic scale factors parametrized to the zero-point energies of small molecules. One is the use of scaling factors via the standard method [56,57,66], as listed in Table S1. The other is reaction-specific scale factors [87,104], which were obtained by using hybrid degeneracy-corrected second-order vibrational perturbation theory [105,106] with the MPW1K/6-311+G(2df,2p)electronic structure method as listed in Table S2.

The torsional anharmonicity was included by the multistructural method with torsional anharmonicity based on a coupled torsional potential [94]. Torsional frequencies are typically low frequencies, and they are scaled (like all other frequencies) prior to applying the multistructural method, which accounts for torsional potential anharmonicity and multiple conformational structures, when present. Note that harmonic potentials have only a single local minimum so the effect of multiple conformational structures may be considered to be an anharmonicity correction.

Electronic structure: Higher-level methods for dynamics

Previous investigations have shown that CCSD(T)-F12a/cc-pVDZ-F12 (Level-1) can predict reliable geometries and zero-point vibrational energies (E_{ZPE}) [66,88–90]. Therefore, for reactions R1a, R1b, R1c, and R2.1, we performed higher-level geometry optimizations and vibrational frequency calculations by using Level-1.

However, the CCSD(T) energies are not expected to be quantitatively reliable because previous investigations have

Table 1. Electronic structure methods and basis sets.

Abbreviation	Explanation	Reference
CCSD(T)	Coupled cluster theory with single and double excitations and quasiperturbative connected triples	[114]
CCSD(T)-F12a	CCSD(T) with explicit correlation of type F12a	[115,116]
DF-CCSD(T)-F12b	CCSD(T) with density fitting and explicit correlation of type F12b	[117]
CCSDT(Q)	Coupled cluster theory with single, double, and triple excitations and quasiperturbative connected quadruples	[118]
CBS	Complete basis set limit obtained by extrapolation	
W2X	A composite method to approximate CCSD(T)/CBS	[107]
W2X+SC [a]	W2X plus a semiempirical correction	
W3X-L	A composite method to approximate CCSDT(Q)/CBS	[107]
revM06	Revised Minnesota-2006 density functional	[119]
M06CR	revM06 density functional reparametrized for Criegee intermediate reactions	[66]
A/B [b]	A calculation with electronic structure approximation A and basis set B	
A/B//C/D [b,c]	A single-point energy calculation with method A/B at a geometry optimized by method C/D and with frequencies by method C/D.	
cc-pVDZ-F12	A polarized valence-double-zeta basis set for explicitly correlated calculations	[120]
jun-cc-pVDZ	A partially augmented polarized valence-double-zeta basis set	[121]
MG3S	A minimally augmented polarized valence-triple-zeta basis set	[122]
Level-1	CCSD(T)-F12a/cc-pVDZ-F12	
Level-2	DF-CCSD(T)-F12b/jun-cc-pVDZ	

[a]SC is a semiempirical correction that is equal to the difference between W3X-L and W2X for the barrier of reaction through **TS-3a**.

[b]For composite methods, A/B becomes A because the basis sets used for individual steps in the calculation are defined as part of the method.

[c]Note that A/B//A/B is abbreviated as A/B; this is called a calculation with a consistently optimized geometry. Note that an A/B///C/D calculation in which A ≠ C and/or B ≠ D is called a single-point energy calculation.

indicated that Criegee intermediates are strongly correlated, which makes it necessary to perform beyond-CCSD(T) calculations in order to obtain reliable single-point energies [56,57,66,87–92]. Therefore, W3X-L//Level-1 was used for single-point energy calculations on reactions R1a and R2.1. Previous validation studies indicate that this puts our results close to the very accurate CCSDT(Q)/CBS level [56,57,66,107].

For R3.1 and R4.1, we performed higher-level geometry optimizations and frequency calculations by DF-CCSD(T)-F12b/jun-cc-pVDZ (Level-2), because this level has been validated in previous [66] investigations of the similar reaction $CH_2OO + (H_2O)_2$. In addition, the reliability of Level-2 is also discussed in the "Electronic energies: Reactions involving 2 water molecules" section.

For the barrier of the transition states of reactions R3.1 and R4.1, we used single-point calculations. For **TS-3a**, we used W3X-L//Level-2 to reach an accuracy close to CCSDT(Q)/CBS. For **TS-3b, TS-3c**, and **TS-3d**, we used W2X//Level-2 + SC. For R3.1, the semiempirical correction was taken to be 0.60 kcal/mol for the transition structures and 0 for reactants. For R4.1, it is 0.83 kcal/mol for transition structures and 0 for reactants.

The empirical correction (0.6 kcal/mol) of R3.1 in the current article is derived from our calculations [W3X-L//DF-CCSD(T)-F12a/jun-cc-pVDZ] obtained for the most stable transition state structure (**TS-3a**) relative to the most stable complex and water (**C-1** + H_2O), and the empirical correction of R4.1 (0.83 kcal/mol) is derived from the most stable transition state structure (**TS-3a**) relative to the most stable reactant [**1** + $(H_2O)_2$] using W3X-L//DF-CCSD(T)-F12a/jun-cc-pVDZ. In comparison, we note that the calculated results in a previous paper [65] show that the beyond-CCSD(T) difference (between W3X-L and W2X) is a very similar 0.72 kcal/mol for different transition states in the $CH_2OO+(H_2O)_2$ reaction. These similarities confirm the reasonableness of these empirical corrections for these specific reactions.

Electronic structure: Lower-level methods for dynamics

The choice of a lower-level method is explained in "Electronic energies: Unimolecular reactions of **1**," "Electronic energies: Bimolecular reactions of *E*-CH_2(OH)CHOO + H_2O," and "Electronic energies: Reactions involving 2 water molecules" sections.

Electronic structure software

For the electronic structure calculations of coupled cluster theory, we used Molpro 2019 [108] and MRCC code [109], while calculations based on density functional theory (DFT) were performed by Gaussian 16 [110].

Results and Discussion

Electronic energies: Unimolecular reactions of 1

There are 5 conformers for **1** as listed in Table S3. The W2X//M06CR/MG3S and M06CR/MG3S methods yield different structures as the global minimum. Here, we used the lowest-energy structure of **1** as obtained by W2X//M06CR/MG3S.

The enthalpy profile of reaction R1 at 0 K as obtained at W3X-L//Level-1 and W2X//Level-1 is depicted in Fig. 2. We found that there are 3 reaction pathways for the unimolecular reactions of *E*-CH_2(OH)CHOO (**1**), in agreement with previous literature [56–62,66,67,91]. They are 1,3-ring closure via reaction R1a for the formation of dioxirane, 1,3-H-transfer via reaction R1b for the formation of **3** + OH [56–62,66,67,91], and a 1,2-insertion of -OH mechanism to produce **4** [62,111].

The activation enthalpy at 0 K ($\Delta H_0^{\ddagger}$) of unimolecular rearrangement R1a is estimated to be 15.19 kcal/mol at W3X-L//Level-1 as depicted Fig. 2, which is 11 to 13 kcal/mol lower than those of reactions R1b and R1c. Therefore, unimolecular reaction of *E*-CH_2(OH)CHOO (**1**) is dominated by **TS-1a**, and we do not consider the reaction pathways **TS-1b** and **TS-1c** in kinetics calculations.

The enthalpy of activation (15.19 kcal/mol) at 0 K for the unimolecular reaction via **TS-1a** is 3.84, 8.51, and 0.44 kcal/mol lower than those of the unimolecular ring closure reactions of CH_2OO, *Z*-CH_3CHOO, and *E*-CH_3CHOO calculated by W3X-L//Level-1 [56]. Moreover, the enthalpy of activation at 0 K via **TS-1a** is 4.41 kcal/mol lower than that of the ring closure reaction of *Z*-CH_2(OH)CHOO calculated by CCSD(T)//M06-2X [62,112]. This shows that the hydroxyl group in *E*-CH_2(OH)CHOO enhances the reactivity for the unimolecular ring closure reaction.

$\Delta H_0^{\ddagger}$ for **TS-1a** (15.19 kcal/mol) is 0.59 kcal/mol higher than the value reported in the literature that was obtained by CCSD(T)//M06-2X [62]. A Boltzmann factor corresponding to 0.59 kcal/mol would decrease the rate constants by a factor of 2.7 at 298 K. Moreover, the beyond CCSD(T) contribution is only 0.12 kcal/mol for **TS-1a** in Table 2, which is much lower than that of the average deviation (0.53 kcal/mol) between W2X and W3X-L in a previous investigation [66]. This shows that the beyond-CCSD(T) contribution is reaction specific, which implies that high-accuracy quantum chemical calculations are needed for obtaining quantitative relative enthalpies of activation.

For reaction R1a, $\Delta H_0^{\ddagger}$ using M11-L/MG3S differs from our best estimate by only 0.09 kcal/mol in Table 2. Thus, we use M11-L/MG3S for direct dynamics calculations for R1a.

Electronic energies: Bimolecular reactions of *E*-CH_2(OH)CHOO + H_2O

As depicted in Fig. 2, 2 different mechanisms, R2.1 and R2.2, are considered for the *E*-CH_2(OH)CHOO (1) + H_2O reaction. Details of the electronic structure calculations for **TS-2a** and **TS-2b** are provided in Table 3 and Table S4.

Our best estimate of $\Delta H_0^{\ddagger}$ for **TS-2a** is −0.09 kcal/mol, which is 1.11 kcal/mol higher than that of the previous investigation [62].

We find that $\Delta H_0^{\ddagger}$ for reaction R2.1 is lower than that for *E*-CH_3CHOO + H_2O by 1.29 kcal/mol at the W3X-L//QCISD/cc-pVDZ level [56]. This again shows that the reaction of *E*-CH_2(OH)CHOO (**1**) with H_2O is enhanced by the introduction of an OH group in Criegee intermediates. The energetically most favorable intermediates have an H-bond that increases their rigidity and thus reduces their contribution to the population.

Table 3 shows that the mean unsigned deviation (MUD) of W2X//Level-1 is 0.65 kcal/mol relative to W3X-L//Level-1 for reaction R2.1; this corresponds to a Boltzmann factor of 3.8 at 240 K. This again shows the need for beyond CCSD(T) calculations.

Table 3 shows that M06CR/MG3S (using the M06CR exchange-correlation functional previously re-parameterized for reactions of Criegee intermediates) performs well in describing

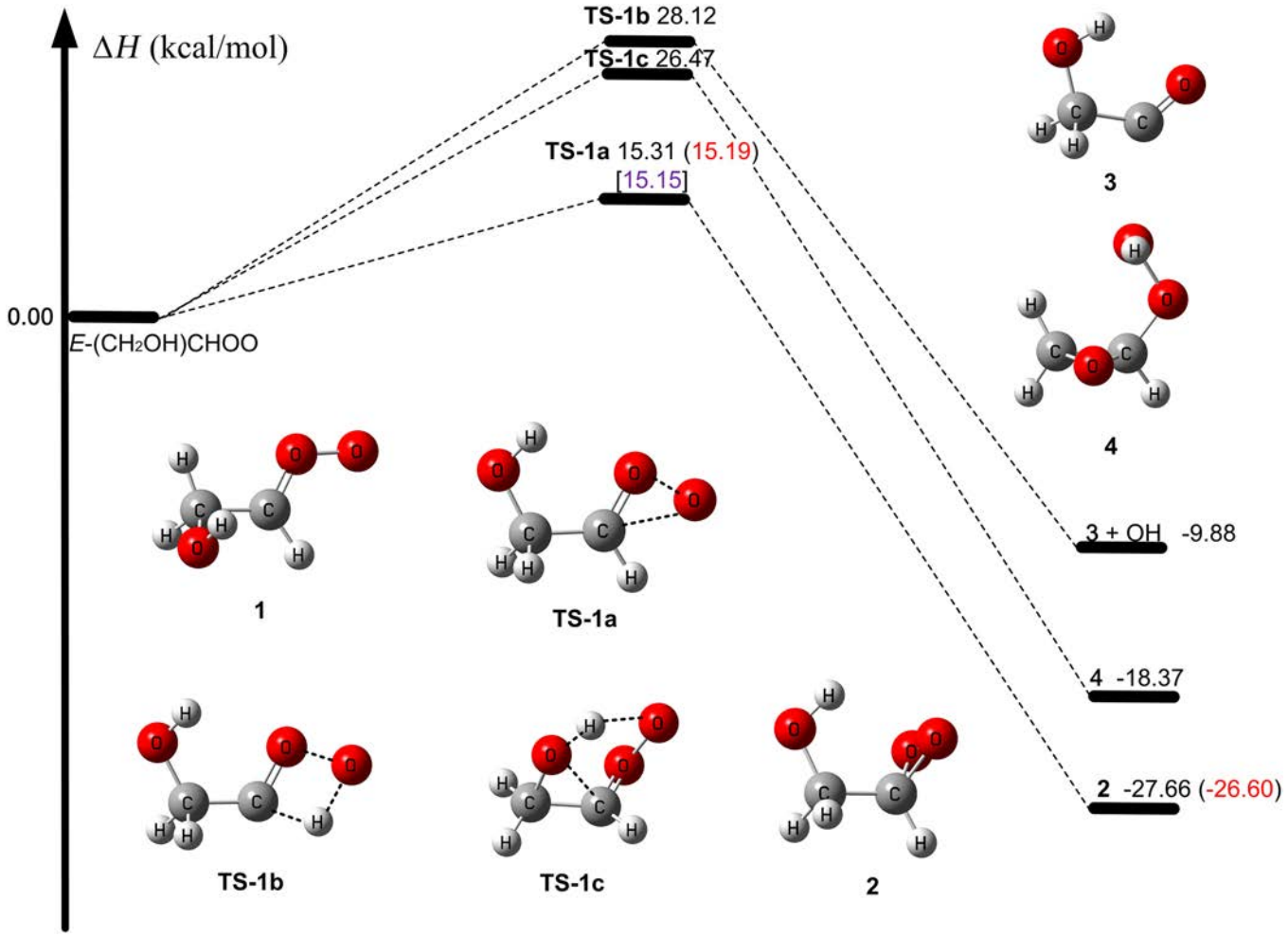


Fig. 2. The relative enthalpy profile at 0 K (in kcal/mol) for unimolecular reactions of **1** calculated by W2X//Level-1. The values in parentheses are obtained using W3X-L//Level-1. The values in brackets are obtained using W3X-L//Level-1 with reaction-specific scale factors.

reaction R2.1, and it significantly exceeds the accuracy of the popular CCSD(T)/CBS level. Therefore, we selected it to do direct dynamics calculations.

One mechanism (R2.1) is an addition coupled to a hydrogen transfer reaction, which is the usual mechanism for reactions of Criegee intermediates with H_2O [56,57,66–69]. It begins with the formation of a pre-reaction hydrogen-bonded complex **C-1**. Table S5 also shows that the W2X//M06CR/MG3S and M06CR/MG3S methods predict the same structure to be the lowest-energy structure of **C-1**. In the next step, **C-1** proceeds through **TS-2a** or **TS-2b** to isomerize into hydroxyl hydroperoxide **5** (see Fig. 3). The 2 transition states, **TS-2a** and **TS-2b,** differ in the orientation of the dangling H of H_2O as shown in Fig. 3.

The other mechanism (reaction R2.2) is a 1,2-insertion of OH catalyzed by water as shown in Fig. 3. Specifically, the complex **C-1** undergoes isomerization via the transition state with transition structures **TS-2c** and **TS-2d**, which differ due to different orientations of H_2O. In **TS-2c**, water acts as a bridge to enable the H atom from the hydroxyl group of **1** to transfer to the terminal oxygen, while simultaneously the oxygen atom of the OH group in **1** attacks the central carbon atom of **1**; this mechanism leads to the formation of **4**.

The most stable transition state of reaction R2.1 is **TS-2a**, and its $\Delta H_0^{\ddagger}$ is 3.06 kcal/mol lower than that of **TS-2c** as calculated by W2X//Level-2 as shown in Fig. 3. Therefore, reaction R2.2 is not considered for kinetics calculations.

We also calculated the barrier for the isomerization of product **5** based on M06CR/MG3S. The results are in Fig. S1, and they show that the decomposition of **5** is not feasible in the atmosphere.

Electronic energies: Reactions involving 2 water molecules

We first confirm the reliability of optimized geometries and calculated zero-point vibrational energies by using DF-CCSD(T)-F12b/jun-cc-pVDZ (Level-2). Our calculated results (see Table 3) show that the difference of MUD in $\Delta H_0^{\ddagger}$ between W2X//Level-1 and W2X//Level-2 is less than 0.01 kcal/mol. This shows that Level-2 can obtain reliable optimized geometries, compared with Level-1. The difference in zero-point vibrational energies (see Table S3) between Level-1 and Level-2 is less than 0.04 kcal. We conclude that Level-2 can produce reliable zero-point vibrational energies, compared with Level-1. The reliability of Level-2 has also been shown for other Criegee reactions [66,88–90]. Therefore, we will use Level-2 to do geometrical optimization and frequency calculations in the reactions involving 2 water molecules.

Table 2. The enthalpy of activation at 0 K ($\Delta H_0^{\ddagger}$ [a] in kcal/mol) calculated for reaction R1a. [a]

Level	**TS-1a**	UD [b]
W3X-L//Level-1 [c]	15.19	0.00
M11-L/MG3S	15.28	0.09
W2X//Level-1	15.31	0.12
CCSD(T)//M06-2X	14.60 [d]	0.59
MN15-L/MG3S	14.49	0.70
M06CR/MG3S	17.21	2.02

[a]$\Delta H_0^{\ddagger}$ is the enthalpy of activation at 0 K. E_{ZPE} is scaled by the generic scale factors.

[b]UD denotes unsigned deviation from the best estimate.

[c]W3X-L//Level-1 is our best estimate for **TS-1a**.

[d]This datum is from [62].

Table 3. The enthalpies of activation at 0 K ($\Delta H_0^{\ddagger}$ in kcal/mol) for reaction R2.1.

Level	**TS-2a**	**TS-2b**	MUD [a]
W3X-L//Level-1 [b]	−0.09	0.60	0.00
M06CR/MG3S	0.20	0.91	0.30
MN15-L/MG3S	−0.65	0.12	0.52
W2X//Level-2	−0.73	0.02	0.65
W2X//Level-1	−0.73	−0.05	0.65
M11-L/MG3S	−0.89	−0.94	1.17

[a]MUD is the mean unsigned deviation from the best estimate.

[b]W3X-L//Level-1 is our best estimate for **TS-2a** and **TS-2b**. E_{ZPE} is scaled by the generic scale factors.

We considered 2 reaction mechanisms for reactions R3 and R4, i.e., reactions R3.1 and R3.2 for R3 and reactions R4.1 and R4.2 for R4.

In reactions R3.1 (see Fig. 4) and R4.1 (see Fig. S2), a water molecule acts as a bridge to catalyze the addition-coupled hydrogen transfer reaction via **TS-3a**, **TS-3b**, **TS-3c**, and **TS-3d**; this mechanism is similar to that for reaction of other Criegee intermediates with $(H_2O)_2$ [66–69]. In R3.1, the reaction occurs by **C-1** colliding with a water monomer responsible for the formation of 2 conformers of *E*-CH_2(OH)CHOO…$(H_2O)_2$, labeled as **C-2** and **C-3**. In addition, C-2 and C-3 can also be formed by a water dimer colliding with *E*-CH_2(OH)CHOO (**1**).

Reactions R3.2 and R4.2 are a 1,2-insertion of the OH group catalyzed by 2 H_2O via **TS-3e**, **TS-3f**, and **TS-3g** as shown in Figs. S3 and S4. In these transition states, the 2 H_2O together act as a bridge to transfer H from OH in Criegee intermediates (a triple H atom transfer process) and concert with the oxygen atom of OH to attack the central carbon atom. However, the lowest transition state (**TS-3e**) of reaction R3.2 is 7.58 kcal/mol higher than that (**TS-3a**) of reaction R3.1 as calculated by M06CR/MG3S (see Table 4 and Fig. S3); this leads to a Boltzmann factor of 8×10^6 at 240 K. Similarly, for R4.2, it is still not feasible in terms of $\Delta H_0^{\ddagger}$ comparing R4.1 (see Fig. S4). Therefore, we do not consider R3.2 and R4.2 for kinetics calculations.

Compared with $CH_2OO + (H_2O)_2$ [66], $\Delta H_0^{\ddagger}$ relative to **1** + $(H_2O)_2$ by W3X-L//Level-2 is 3.6 kcal/mol lower than that of $CH_2OO + (H_2O)_2$ calculated by using W3X-L//CCSD(T)-F12a/cc-pVTZ-F12 level [66].

For direct dynamics calculations of the kinetics, we made a semiempirical correction (SC) to better select the functional with the best performance. Table 4 shows that compared to the results of SC+W2X//Level-2, MUD (R3.1) of $\Delta H_0^{\ddagger}$ is 0.57 kcal/mol using M06CR/MG3S. The imaginary frequencies are also listed in Table S6, where they are compared to the results obtained with Level-2; MUD between Level-2 (best estimate) and M06CR/MG3S for the 4 transition structures is only 45i cm^{-1}. This supports using M06CR/MG3S for direct dynamics calculations of **C-1** + H_2O and **1** + $(H_2O)_2$ (R3.1 and R4.1).

Effect of anharmonicity on activation enthalpy

Tables S1 and S2 show that the reaction-specific scale factors for **TS-3a** (0.966), **TS-3b** (0.956), **TS-3c** (0.958), and **TS-3d** (0.963) differ very significantly from the generic scale factor (0.981 for Level-2). Table S7 shows that for many channels, this makes a significant change in the calculated enthalpy of activation. For example, $\Delta H_0^{\ddagger}$ of **TS-3b** for reaction R3.1 is decreased by 1.61 kcal/mol, when anharmonicity is calculated using reaction-specific scale factors; this shows the importance of anharmonicity for controlling rate constants in atmospheric chemistry.

Kinetics

Reaction R1 refers to the sum of reactions R1a, R1b, and R1c, but since we will see that pathways 1b and 1c have much higher barriers than 1a, our rate constant k_1 for reaction R1 will be limited to pathway 1a. We will see that our calculations predict that the lowest-energy transition state of reaction R2.1 is ~3 kcal/mol lower than that of reaction R2.2, and so, we will not consider kinetics for reaction R2.2. Reaction R3 refers to the sum of R3.1 and R3.2, and reaction R4 refers to the sum of reactions R4.1 and R4.2. We will see that reactions R3.2 and R4.2 and reaction paths through transition states **TS-3e**, **TS-3f**, and **TS-3g** make insignificant contributions to the rates, and therefore, we will calculate the rate constants of R3 and R4 by considering only mechanisms R3.1 and R4.1 and only transition states **TS-3a**, **TS-3b**, **TS-3c**, and **TS-3d** for these mechanisms. In dynamics calculations on reactions R3.1 and R4.1, we consider both reaction through the loose transition state leading from **1** + $(H_2O)_2$ to **C-2**/**C-3** and reaction through the tight transition states **TS-3a**, **TS-3b, TS-3c,** and **TS-3d**. However, only tight transition states are considered for dynamics calculations on other reactions in this work.

We also consider the pressure effects on the unimolecular reaction of *E*-CH_2(OH)CHOO (**1**) in R1a.

Table 5 and Tables S8 to S20 provide rate constants. It can be seen from Table 5 that $k_{3.1}$ and $k_{4.1}$ are much greater than k_2, and this has the effect that bimolecular reactions involving 2

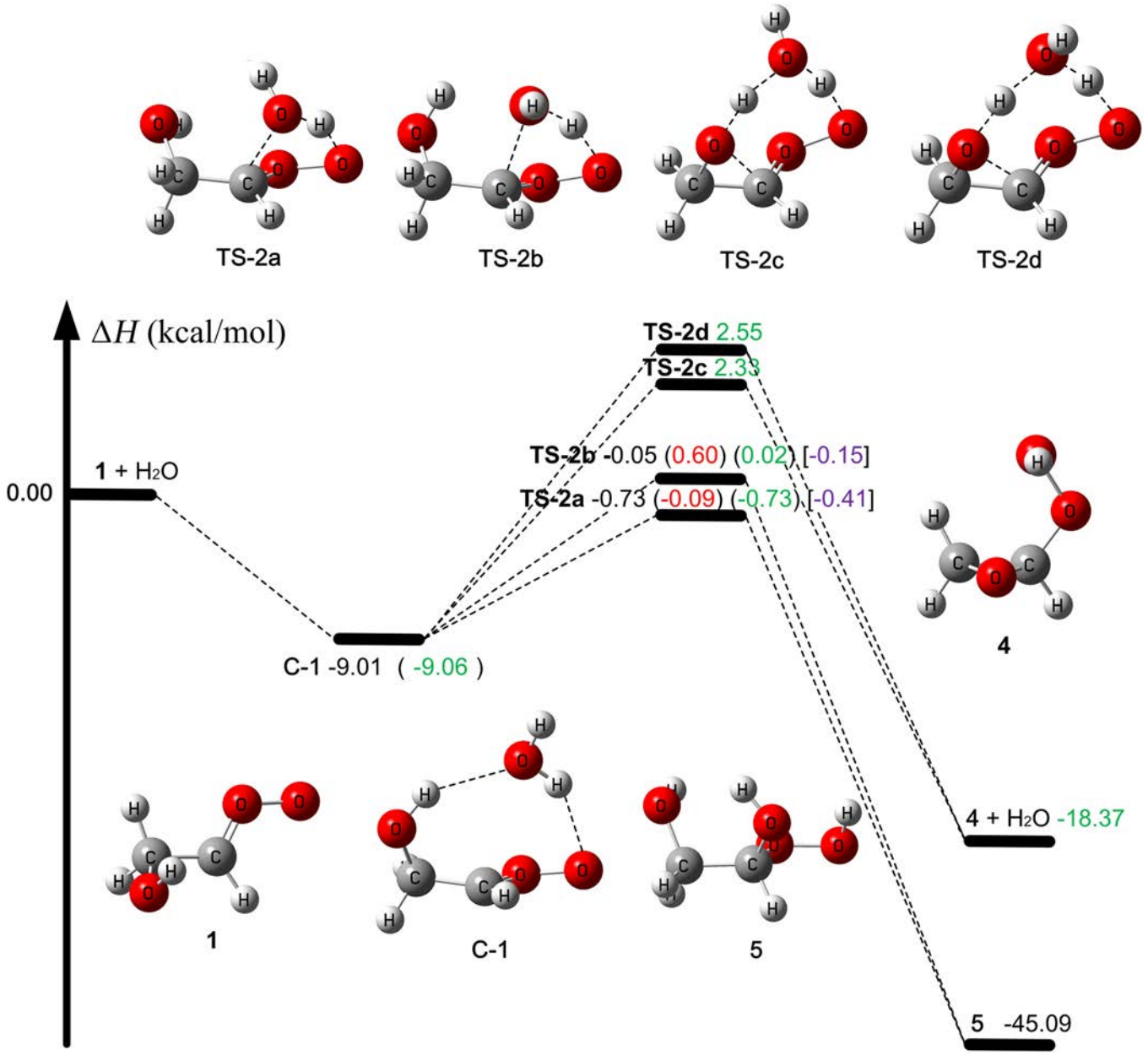


Fig. 3. The relative enthalpy profile at 0 K (in kcal/mol) for **1** + H_2O. The black value is calculated using W2X//Level-1. The red values in parentheses are the enthalpies of activation at 0 K calculated by W3X-L//Level-1. The green values come from W2X//Level-2. The values in brackets are obtained using W3X-L//Level-1 with reaction-specific scale factors.

water molecules are more important than those involving only one water. We fitted the rate constants to [113]

$$k = A\left(\frac{T+T_0}{300}\right)^n \exp\left[-\frac{E(T+T_0)}{R(T^2+T_0^2)}\right] \quad (6)$$

where R is the gas constant (1.987212×10^{-3} kcal mol^{-1} K^{-1}) and A, n, T_0, and E are fitted parameters for each reaction and are listed in Table S21. We also calculated the Arrhenius activation energies E_a (which are local slopes of Arrhenius plots) of each reaction at 190 to 350 K by

$$E_a = \frac{E(T^4 + 2T_0T^3 - T_0^3T^2)}{(T^2+T_0^2)^2} + \frac{nRT^2}{T+T_0} \quad (7)$$

and the results are presented in Table S22.

The reaction rate of **1** with H_2O is expressed by

$$v_1 = -\frac{d[E-CH_2(OH)CHOO]}{dt} = K_{eq1}k_{3.1}[H_2O][H_2O][E-CH_2(OH)CHOO] \quad (8)$$

where K_{eq1} is the equilibrium constants for forming complex **C-1** and $k_{3.1}$ is the bimolecular rate constant of **C-1** + H_2O (R3.1). The reaction rate of **1** + $(H_2O)_2$ is expressed by

$$v_2 = -\frac{d[E-CH_2(OH)CHOO]}{dt} = K_{eq2}k_{4.1}[H_2O][H_2O][E-CH_2(OH)CHOO] \quad (9)$$

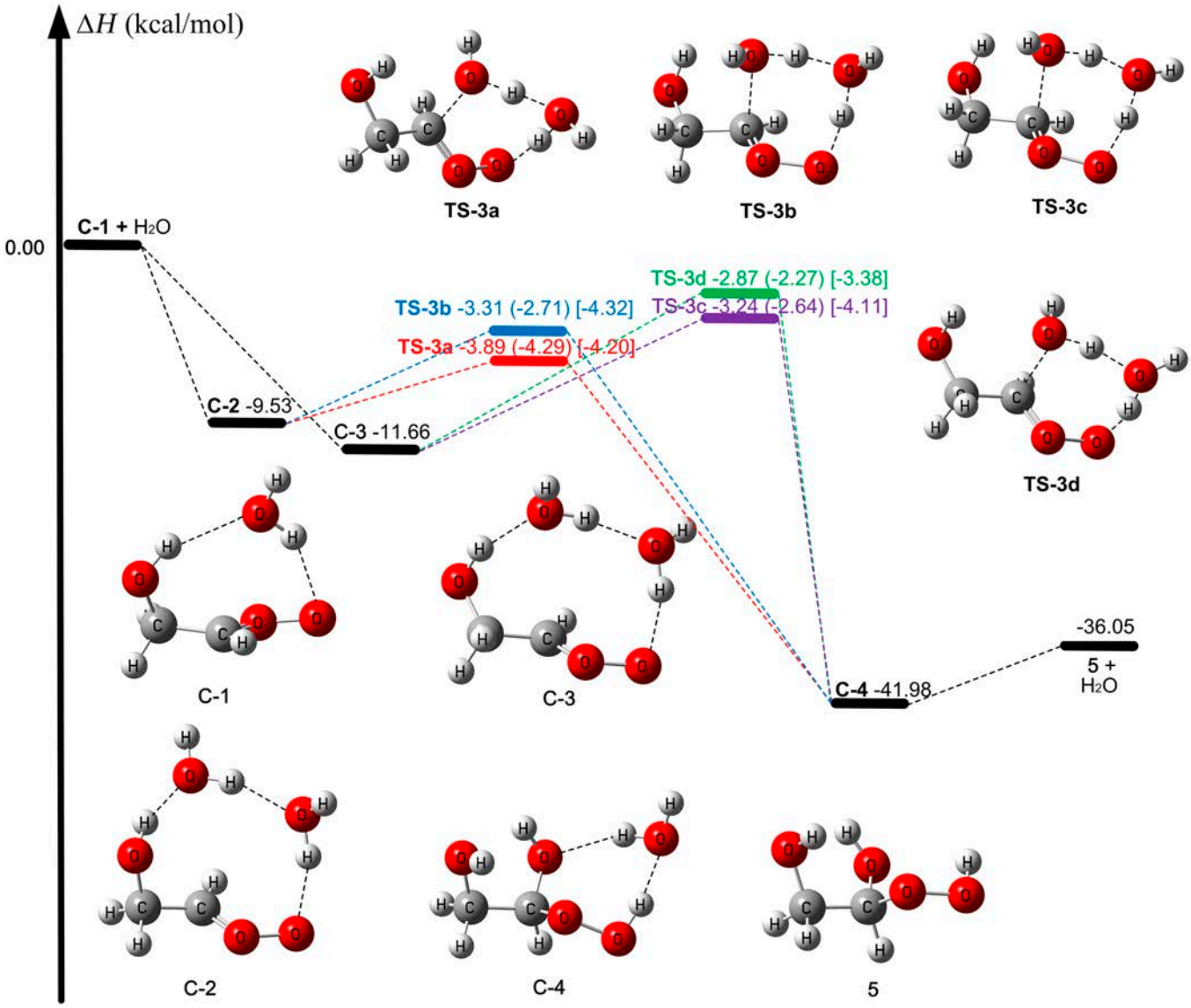


Fig. 4. Relative enthalpy (0 K) with respect to **C-1** and H_2O (in kcal/mol). All values were calculated by W2X//Level-2 except that the results in parentheses are obtained by W3X-L//Level-2 for **TS-3a** and by SC+W2X//Level-2 for **TS-3b**, **TS-3c**, and **TS-3d**. The values in brackets are obtained using SC+W2X//Level-2 with reaction-specific scale factors.

where K_{eq2} is the equilibrium constants for forming $(H_2O)_2$ and $k_{4.1}$ is the bimolecular rate constant of **1** + $(H_2O)_2$ (R4.1). The rate ratio (v_1/v_2) is defined by

$$\frac{v_1}{v_2} = \frac{K_{eq1}k_{3.1}}{K_{eq2}k_{4.1}} \quad (10)$$

and is given in Table 6, where for each altitude we use the temperature of a standard atmosphere at that altitude.

We find that the overall rate (v_1) through R3.1 is much faster than that (v_2) through R4.1 at low temperature, with factors of 4,115 and 796 at 229.7 and 212.6 K, respectively. However, Table 6 shows that v_1 and v_2 are closer at higher temperature, with values decreasing from 35.7 at 249.9 K to 1.27 at 288.8 K.

The complexes formed by Criegee intermediates and water monomer may react with water monomer more rapidly than Criegee intermediates react directly with atmospheric water dimers, and this phenomenon may be common in many similar reactions of Criegee intermediates with 2 water molecules. For example, E-$CH_3CHOO^{\cdots}H_2O + H_2O$ may be more important than E-$CH_3CHOO + (H_2O)_2$ at low temperatures. This has been not considered in the literature [67,68].

Tables S8 to S18 also provide the transmission coefficients and the multistructural torsional anharmonicity factors (F_{act}). For **TS-1a**, we find that recrossing effects decrease the rate constants by only about 1%. The torsional anharmonicity of **TS-1a** increases the rate constant by 50% to 80%.

For R2.1, the torsional anharmonicity decreases the rate constants by about 40% for **TS-2a** and increases them by 15% to 31% for **TS-2b**. Recrossing effects for **TS-2b** cause the rate constant to drop by roughly 30% at 298 K.

For reaction R3.1, the effects of these 3 factors are larger. For example, at 298 K, torsional anharmonicity and recrossing effects for **TS-3a** decrease the rate constant by 39% and 47%, respectively, while tunneling effects increase the rate by a factor of approximately 2.

To consider whether tunneling is fast enough to allow reaction R3.2 to compete with reaction R3.1, we calculated tunneling

Table 4. The enthalpies of activation (kcal/mol) at 0 K ($\Delta H_0^{\ddagger}$ [a] in kcal/mol) for reaction R3.1 of **C-1** + H_2O calculated at 4 transition states. [a]

Level	**TS-3a**	**TS-3b**	**TS-3c**	**TS-3d**	MUD [b]
SC+W2X//Level-2 [c]	−3.29	−2.71	−2.64	−2.27	0.00
M06CR/MG3S	−2.64	−2.14	−2.15	−1.69	0.57
W2X//Level-2	−3.89	−3.31	−3.24	−2.87	0.60
M11-L/MG3S	−2.26	−2.02	−2.02	−1.06	0.89
MN15-L/MG3S	2.38	2.74	2.86	3.40	5.57

[a] $\Delta H_0^{\ddagger}$ is the enthalpy of activation at 0 K relative to **C-1** + H_2O. E_{ZPE} is scaled by the generic scale factors.

[b] MUD denotes mean unsigned deviation from the best estimate (SC+W2X//Level-2).

[c] SC+W2X//Level-2 includes the semiempirical correction (SC), which equals $\Delta H_0^{\ddagger}$ result for **TS-3a** relative to **C-1** + H_2O using W3X-L//Level-2 minus $\Delta H_0^{\ddagger}$ for **TS-3a** relative to **C-1** + H_2O using W2X//Level-2. By this definition, SC+W2X//Level-2 is the same as to W3X-L//Level-2 for $\Delta H_0^{\ddagger}$ of **TS-3a** relative to **C-1** + H_2O.

Table 5. Rate constants in the high-pressure limit [a,b] as calculated with reaction-specific scale factors.

T/K	k_1 [a]	k_2 [a]	$k_{3.1}$	$k_{4.1}$ [a]
220	5.81×10^{-3}	6.88×10^{-14}	8.54×10^{-10}	9.07×10^{-10}
230	2.66×10^{-2}	5.95×10^{-14}	7.20×10^{-10}	9.02×10^{-10}
250	3.92×10^{-1}	4.67×10^{-14}	2.61×10^{-10}	8.89×10^{-10}
270	3.92×10^{0}	3.84×10^{-14}	6.22×10^{-11}	8.25×10^{-10}
290	2.87×10^{1}	3.29×10^{-14}	1.85×10^{-11}	5.69×10^{-10}
298	5.93×10^{1}	3.12×10^{-14}	1.24×10^{-11}	4.25×10^{-10}
300	7.06×10^{2}	3.07×10^{-14}	1.13×10^{-11}	3.91×10^{-10}
320	3.62×10^{2}	2.75×10^{-14}	4.99×10^{-12}	1.44×10^{-10}
350	2.97×10^{3}	2.41×10^{-14}	1.95×10^{-12}	3.12×10^{-11}

[a] k_1, k_2, $k_{3.1}$, and $k_{4.1}$ are rate constants for reactions R1, R2, R3.1, and R4.1, respectively. The units are s^{-1} for the unimolecular reaction (k_1) and cm^3 molecule^{-1} s^{-1} for the bimolecular reactions (the other 3).

[b] The rate constants in this table are all are obtained by the dual-level strategy, and the results of higher- and lower-level calculations can be found in the Supplementary Materials (see Tables S8 to S20).

transmission coefficient for the reaction path through **TS-2c**, and the results are listed in Table S23. This calculation shows that although tunneling increases the rate through **TS-3c** by a factor of 17 at 190 K, this is not enough to overcome the difference of $\Delta H_0^{\ddagger}$ (a Boltzmann factor of 3,309 at 190 K when comparing **TS-2c** and **TS-1a**). For this reason, it is not necessary to include **TS-2c** and **TS-2d** in the kinetics calculations.

Tables S8 to S18 show that anharmonicity has a very large effect on quantitative rate prediction. For example, for reaction R3.1 through transition state **TS-3b**, the rate calculated using reaction-specific scale factors is 12 to 77 times faster than the rate calculated using generic scale factors at 190 to 350 K (see Table S12).

The rate constants for R1a and R2.1 calculated in a previous investigation [62] are 2.4 and 6.1 times faster, respectively, than the values in the present work at 298 K. We find that the reaction rate of reaction R2.1 (3.12×10^{-14} cm^3 molecule^{-1} s^{-1} at 298 K in this work) is larger than the reaction rates of CH_2OO, *Z*-CH_3CHOO, and *E*-CH_3CHOO with H_2O (2.4×10^{-16}, 1.9×10^{-19}, and 5.2×10^{-15} cm^3 molecule^{-1} s^{-1} at 298 K, respectively) [56], and this results in a shorter atmospheric lifetime for the present reactant. Therefore, water vapor is regarded as a more important sink for **1** than for the Criegee intermediates without a hydroxy substituent.

The RRKM/ME and SS-QRRK method give almost the same results in Tables S24 and S25. Therefore, we use the SS-QRRK results to consider the pressure dependence. For the unimolecular reaction (**TS-1a**) of **1**, Table S26 shows that the transition pressure, which is defined as the pressure at which the unimolecular rate constant is half of the high-pressure-limit value, changes from 1.3×10^{-3} bar to 0.11 bar over the temperature range from 200 to 350 K. This indicates that the pressure dependence should be considered under atmospheric conditions, that is, one should consider both the temperature dependence and the pressure dependence, as given in Tables S24 to S26.

Atmospheric implications

Table 7 gives the lifetimes of *E*-CH_2(OH)CHOO (**1**) with respect to its unimolecular isomerization R1a (τ_1) and with respect to

Table 6. Equilibrium constants and the rate ratio.

Height (km) [a]	T (K) [a]	K_{eq1} [b]	K_{eq2} [c]	v_1/v_2
0	288.8	6.76×10^{-20}	2.44×10^{-21}	1.27
5	259.3	3.87×10^{-19}	4.62×10^{-21}	11.6
10	229.7	5.58×10^{-18}	1.05×10^{-20}	4,115
15	212.6	1.65×10^{-17}	1.90×10^{-20}	796
20	215.5	1.23×10^{-17}	1.71×10^{-20}	595
25	218.6	9.20×10^{-18}	1.53×10^{-20}	447
30	223.7	5.77×10^{-18}	1.29×10^{-20}	274
35	235.1	2.25×10^{-18}	8.93×10^{-21}	96.1
40	249.9	7.14×10^{-19}	5.87×10^{-21}	35.7
45	266.1	2.48×10^{-19}	3.95×10^{-21}	6.75
50	271.0	1.83×10^{-19}	3.49×10^{-21}	4.73

[a]Data are from [65].

[b]K_{eq1} is the equilibrium constant between **C-1** and **1** + H_2O (in molecules cm^{-3}). For the calculation of this equilibrium constant, we considered all the conformers; details are given in the Supplementary Materials (see Table S5).

[c]K_{eq2} is the equilibrium constant between water dimer and water monomer from the literature in our previous investigation (in molecules cm^{-3}) [123].

Table 7. Atmospheric lifetime as a function of height. [a]

h (km) [a]	T (K) [a]	P (mbar) [a]	$[H_2O]$ [a]	τ_1(s) [b]	τ_2(s) [b]	$\tau_{3.1}$(s) [b]	$\tau_{4.1}$(s) [b]
0	288.8	1,013.25	4.40×10^{17}	4.05×10^{-2}	6.86×10^{-5}	3.06×10^{-6}	3.88×10^{-6}
5	259.3	542	1.70×10^{16}	8.44×10^{-1}	1.39×10^{-3}	7.17×10^{-5}	8.36×10^{-4}
10	229.7	269	3.00×10^{14}	4.05×10^{1}	5.58×10^{-2}	2.77×10^{-3}	1.14×10^{0}

[a]The temperature (T) and pressure (P) as functions of height (h) and water concentrations (molecules cm^{-3}) are from [65]. [b]The lifetimes of E-CH2(OH)CHOO with respect to its unimolecular isomerization by reaction R1a (τ1) and with respect reactions R2.1 (τ2), R3.1(τ3.1), and R4.1(τ4.1).

the reactions involving R2.1 (τ_2), R3.1($\tau_{3.1}$), and R4.1($\tau_{4.1}$). The lifetimes with respect to the bimolecular reactions are given by

$$\tau_2 = \frac{1}{k_2[H_2O]} \quad (11)$$

for reaction with H_2O, by

$$\tau_{3.1} = \frac{1}{K_{eq1}k_{3.1}[H_2O]^2} \quad (12)$$

for the **C-1** + H_2O reaction, and by

$$\tau_{4.1} = \frac{1}{K_{eq2}k_{4.1}[H_2O]^2} \quad (13)$$

for the **1** + $(H_2O)_2$ reaction. The atmospheric lifetime τ_2 is changed from 6.9×10^{-5} to 5.6×10^{-2} s as the altitude is increased from sea level to 10 km, whereas the atmospheric lifetimes of **1** with respect to R3.1 ($\tau_{3.1}$) and R4.1 ($\tau_{4.1}$) are even shorter: 3.1×10^{-6} s to 2.8×10^{-3} s and 3.8×10^{-6} s to 1.1 s at heights below 10 km. The atmospheric lifetime relative to isomerization (τ_1) changes from 4.0×10^{-2} s to 4.0×10^{1} s over the 0- to 10-km range. This shows that **1** is mainly removed by **C-1** + H_2O and **1** + $(H_2O)_2$.

In addition, the internal rotation channel may reinforce the pressure effects of the unimolecular reactions of **1** to further decrease the rate constant of unimolecular reactions [88]. However, the unimolecular reactions are not a major sink of **1**. Thus, we do not further consider this point.

Conclusions

In this work, we use high-level coupled cluster theory and multi-structural canonical VTST with small-curvature tunneling to investigate the unimolecular reactions of *E*-CH_2(OH)CHOO (**1**) and the bimolecular reactions of **1** with H_2O, of *E*-CH_2(OH)CHOO…H_2O (**C-1**) with H_2O, and of **1** with $(H_2O)_2$. We find that the beyond-CCSD(T) contribution to the energetics depends on the specific reaction. The calculated results show that the introduction of the OH group enhances the reactivity of the Criegee intermediate.

The present findings help to elucidate the dominant sink of *E*-CH_2(OH)CHOO (**1**) by water vapor. We find that **1** + $(H_2O)_2$ and **C-1** + H_2O are the most important loss process of **1** in the atmosphere. In addition, the present findings show that **C-1** + H_2O is more important than **1** + $(H_2O)_2$ at low temperatures.

Our investigation also shows that for R2, R3.1, and R4.1, anharmonicity is a key parameter for obtaining quantitative rate constants.

The results for R1a and R2.1 calculated in [62] are 2.4 and 6.1 times faster, respectively, than the values in our quantitative results at 298 K. These errors are all within the uncertainty range of the predictions as described in [62], thus confirming the expected qualitative reliability of the structure–activity relations (SARs) from [62]. Future application of SARs for qualitative prediction may be reasonable.

Acknowledgments

Funding: This work was supported in part by the National Natural Science Foundation of China (42120104007, 41775125, and 91961123), by Guizhou Provincial Science and Technology Projects, China (CXTD [2022]001), by the Science and Technology Foundation of Guizhou Provincial Department of Education, China (no. KY[2021]014), and by the U.S. Department of Energy, Office of Science, Office of Basic Energy Sciences under Award DE-SC0015997. **Author contributions**: Y.S. and B.L. calculated the data of this article. Y.S. wrote the first draft of the manuscript. B.L. and D.G.T. planned the research, analyzed the results, and revised the article. **Competing interests**: The authors declare that they have no competing interests.

Data Availability

Data are available in the Supplementary Materials.

Supplementary Materials

Details of dual-level calculations of high-pressure-limit rate constants
Details of the variable reaction coordinate rate calculations
Table A1
Tables S1 to S28
Figs. S1 to S13

References

1. Criegee R. Mechanism of ozonolysis. *Angew Chem Int Ed*. 1975;14(11):745–752.
2. Harrison RM, Yin J, Tilling RM, Cai X, Seakins PW, Hopkins JR, Lansley DL, Lewis AC, Hunter MC, Heard DE, et al. Measurement and modelling of air pollution and atmospheric chemistry in the U.K. West Midlands conurbation: Overview of the PUMA Consortium project. *Sci Total Environ*. 2006;360 (1–3):5–25.
3. Chuong B, Zhang J, Donahue NM. Cycloalkene ozonolysis: Collisionally mediated mechanistic branching. *J Am Chem Soc*. 2004;126(39):12363–12373.
4. Johnson D, Marston G. The gas-phase ozonolysis of unsaturated volatile organic compounds in the troposphere. *Chem Soc Rev*. 2008;37(4):699–716.
5. Atkinson R, Aschmann SM, Arey J, Shorees B. Formation of OH radicals in the gas phase reactions of O_3 with a series of terpenes. *J Geophys Res*. 1992;97(D5):6065–6073.
6. Paulson SE, Chung MY, Hasson AS. OH radical formation from the gas-phase reaction of ozone with terminal alkenes and the relationship between structure and mechanism. *J Phys Chem A*. 1999;103(41):8125–8138.
7. Liu F, Beames JM, Petit AS, McCoy AB, Lester MI. Infrared-driven unimolecular reaction of CH_3CHOO Criegee intermediates to OH radical products. *Science*. 2014;345(6204):1596–1598.
8. Hansen AS, Liu Z, Chen S, Schumer MG, Walsh PJ, Lester MI. Unraveling conformer-specific sources of hydroxyl radical production from an isoprene-derived Criegee intermediate by deuteration. *J Phys Chem A*. 2020;124(124):4929–4938.
9. Li Y-L, Kuo M-T, Lin JJ-M. Unimolecular decomposition rates of a methyl-substituted Criegee intermediate *syn*-CH_3CHOO. *RSC Adv*. 2020;10(14):8518–8524.
10. Kidwell NM, Li H, Wang X, Bowman JM, Lester MI. Unimolecular dissociation dynamics of vibrationally activated CH_3CHOO Criegee intermediates to OH radical products. *Nat Chem*. 2016;8(5):509–514.
11. Green AM, Barber VP, Fang Y, Klippenstein SJ, Lester MI. Selective deuteration illuminates the importance of tunneling in the unimolecular decay of Criegee intermediates to hydroxyl radical products. *Proc Natl Acad Sci USA*. 2017;114(47):12372–12377.
12. Barber VP, Pandit S. Four-carbon Criegee intermediate from isoprene ozonolysis: Methyl vinyl ketone oxide synthesis, infrared spectrum, and OH production. *J Am Chem Soc*. 2018;140(34):10866–10880.
13. Lester MI, Klippenstein SJ. Unimolecular decay of Criegee intermediates to OH radical products: Prompt and thermal decay processes. *Acc Chem Res*. 2018;51(4):978–985.
14. Novelli A, Vereecken L, Lelieveld J, Harder H. Direct observation of OH formation from stabilised Criegee intermediates. *Phys Chem Chem Phys*. 2014;16(37):19941–19951.
15. Xu K, Wang W, Wei W, Feng W, Sun Q, Li P. Insights into the reaction mechanism of Criegee intermediate CH_2OO with methane and implications for the formation of methanol. *J Phys Chem A*. 2017;121(38):7236–7245.
16. Chhantyal-Pun R, Shannon RJ, Tew DP, Caravan RL, Duchi M, Wong C, Ingham A, Feldman C, McGillen MR, Khan MAH, et al. Experimental and computational studies of Criegee intermediate reactions with NH_3 and CH_3NH_2. *Phys Chem Chem Phys*. 2019;21(26):14042–14052.
17. Vereecken L, Harder H, Novelli A. The reaction of Criegee intermediates with NO, RO_2, and SO_2, and their fate in the atmosphere. *Phys Chem Chem Phys*. 2012;14(42):14682–14695.
18. Caravan RL, Khan MAH, Rotavera B, Papajak E, Antonov IO, Chen MW, Au K, Chao W, Osborn DL, Lin JJM, et al. Products of Criegee intermediate reactions with NO_2: Experimental measurements and tropospheric implications. *Faraday Discuss*. 2017;200:313–330.
19. Mauldin RL III, Berndt T, Sipilä M, Paasonen P, Petäjä T, Kim S, Kurtén T, Stratmann F, Kerminen V-M, Kulmala M. A new atmospherically relevant oxidant of sulphur dioxide. *Nature*. 2012;488:193–196.

20. Aroeira GJR, Abbott AS, Elliott SN, Turney JM, Schaefer HF. The addition of methanol to Criegee intermediates. *Phys Chem Chem Phys*. 2019;21(32):17760–17771.
21. Chung C-A, Su JW, Lee Y-P. Detailed mechanism and kinetics of the reaction of Criegee intermediate CH_2OO with HCOOH investigated via infrared identification of conformers of hydroperoxymethyl formate and formic acid anhydride. *Phys Chem Chem Phys*. 2019;21(38):21445–21455.
22. Tadayon SV, Foreman ES, Murray C. Kinetics of the reactions between the Criegee Iintermediate CH_2OO and alcohols. *J Phys Chem A*. 2018;122(1):258–268.
23. Osborn DL, Taatjes CA. The physical chemistry of Criegee intermediates in the gas phase. *Int Rev Phys Chem*. 2015;34(3):309–360.
24. Vereecken L, Francisco JS. Theoretical studies of atmospheric reaction mechanisms in the troposphere. *Chem Soc Rev*. 2012;41(19):6259–6293.
25. Kukui A, Chartier M, Wang J, Chen H, Dusanter S, Sauvage S, Michoud V, Locoge N, Gros V, Bourrianne T, et al. Role of Criegee intermediates in the formation of sulfuric acid at a Mediterranean (Cape Corsica) site under influence of biogenic emissions. *Atmos Chem Phys*. 2021;21(17):13333–13351.
26. Boy M, Mogensen D, Smolander S, Zhou L, Nieminen T, Paasonen P, Plass-Dülmer C, Sipilä M, Petäjä T, Mauldin L, et al. Oxidation of SO_2 by stabilized Criegee intermediate (SCI) radicals as a crucial source for atmospheric sulfuric acid concentrations. *Atmos Chem Phys*. 2013;13(7):3865–3879.
27. Kim S, Guenther A, Lefer B, Flynn J, Griffin R, Rutter AP, Gong L, Cevik BK. Potential role of stabilized Criegee radicals in sulfuric acid production in a high biogenic VOC environment. *Environ Sci Technol*. 2015;49(6):3383–3391.
28. Ahrens J, Carlsson PTM, Hertl N, Olzmann M, Pfeifle M, Lennard Wolf J, Zeuch T. Infrared detection of Criegee intermediates formed during the ozonolysis of β-pinene and their reactivity towards sulfur dioxide. *Angew Chem Int Ed*. 2014;53(3):715–719.
29. Heaton KJ, Sleighter RL, Hatcher PG, Hall WA IV, Johnston MV. Composition domains in monoterpene secondary organic aerosol. *Environ Sci Technol*. 2009;43(20):7797–7802.
30. Bonn B, Schuster G, Moortgat GK. Influence of water vapor on the process of new particle formation during monoterpene ozonolysis. *J Phys Chem A*. 2002;106(12):2869–2881.
31. Nguyen TB, Tyndall GS, Crounse JD, Teng AP, Bates KH, Schwantes RH, Coggon MM, Zhang L, Feiner P, Milller DO, et al. Atmospheric fates of Criegee intermediates in the ozonolysis of isoprene. *Phys Chem Chem Phys*. 2016;18(15):10241–10254.
32. Chhantyal-Pun R, Rotavera B, McGillen MR, Khan MAH, Eskola AJ, Caravan RL, Blacker L, Tew DP, Osborn DL, Percival CJ, et al. Criegee intermediate reactions with carboxylic acids: A potential source of secondary organic aerosol in the atmosphere. *ACS Earth Space Chem*. 2018;2(8):833–842.
33. Yao L, Ma Y, Wang L, Zheng J, Khalizov A, Chen M, Zhou Y, Qi L, Cui F. Role of stabilized Criegee intermediate in secondary organic aerosol formation from the ozonolysis of α-cedrene. *Atmos Environ*. 2014;94:448–457.
34. Bagchi A, Yu Y, Huang J-H, Tsai C-C, Hu W-P, Wang CC. Evidence and evolution of Criegee intermediates, hydroperoxides and secondary organic aerosols formed via ozonolysis of α-pinene. *Phys Chem Chem Phys*. 2020;22:(12)6528–6537.
35. Chao W, Hsieh J-T, Chang C-H, Lin JJ-M. Direct kinetic measurement of the reaction of the simplest Criegee intermediate with water vapor. *Science*. 2015;347:(6223)751–754.
36. Vereecken L, Glowacki DR, Pilling MJ. Theoretical chemical kinetics in tropospheric chemistry: Methodologies and applications. *Chem Rev*. 2015;115(10):4063–4114.
37. Watson NAI, Black JA, Stonelake TM, Knowles PJ, Beames JM. An extended computational study of Criegee intermediate–alcohol reactions. *J Phys Chem A*. 2019;123(1):218–229.
38. McGillen MR, Curchod BFE, Chhantyal-Pun R, Beames JM, Watson N, Khan MAH, McMahon L, Shallcross DE, Orrr-Ewing AJ. Criegee intermediate–alcohol reactions, a potential source of functionalized hydroperoxides in the atmosphere. *ACS Earth Space Chem*. 2017;1(10):664–672.
39. Taatjes CA. Criegee intermediates: What direct production and detection can teach us about reactions of carbonyl oxides. *Annu Rev Phys Chem*. 2017;68(1):183–207.
40. Lee Y-P. Perspective: Spectroscopy and kinetics of small gaseous Criegee intermediates. *J Chem Phys*. 2015;143(2):Article 020901.
41. Cox RA, Ammann M, Crowley JN, Herrmann H, Jenkin ME, McNeill VF, Mellouki A, Troe J, Wallington TJ. Evaluated kinetic and photochemical data for atmospheric chemistry: Volume VII—Criegee intermediates. *Atmos Chem Phys*. 2020;20(21):13497–13519.
42. Grira A, Amarandei C, Roman C, Bejaoui O, Aloui N, El Dib G, Arsene C, Bejan IG, Olariu RI, Canosa A, et al. Gas-phase ozone reaction kinetics of C_5–C_8 unsaturated alcohols of biogenic interest. *J Phys Chem A*. 2022;126(27):4413–4423.
43. O'Dwyer MA, Carey TJ, Healy RM, Wenger JC, Picquet-Varrault B, Doussin JF. The gas-phase ozonolysis of 1-penten-3-ol, (z)-2-penten-1-ol and 1-penten-3-one: Kinetics, products and secondary organic aerosol formation. *Z Phys Chem*. 2010;224(7-8):1059–1080.
44. Grosjean D, Grosjean E. Carbonyl products of the ozone-unsaturated alcohol reaction. *J Geophys Res*. 1995;100(D11):22815–22820.
45. Grosjean E, Grosjean D. The reaction of unsaturated aliphatic oxygenates with ozone. *J Atmos Chem*. 1999;32(2):205–232.
46. Elakiya C, Shankar R, Vijayakumar S, Kolandaivel P. A theoretical study on the reaction mechanism and kinetics of allyl alcohol (CH_2=$CHCH_2OH$) with ozone (O_3) in the atmosphere. *Mol Phys*. 2017;115(7):895–911.
47. Kesselmeier J, Staudt M. Biogenic volatile organic compounds (VOC): An overview on emission, physiology and ecology. *J Atmos Chem*. 1999;33(1):23–88.
48. Kirstine W, Galbally I, Ye Y, Hooper M. Emissions of volatile organic compounds (primarily oxygenated species) from pasture. *J Geophys Res*. 1998;103(D9):10605–10619.
49. Kirstine WV, Galbally IE. A simple model for estimating emissions of volatile organic compounds from grass and cut grass in urban airsheds and its application to two Australian cities. *J Air Waste Manage Assoc*. 2004;54(10):1299–1311.
50. Heiden AC, Kobel K, Langebartels C, Schuh-Thomas G, Wildt J. Emissions of oxygenated volatile organic compounds from plants Part I: Emissions from lipoxygenase activity. *J Atmos Chem*. 2003;45(2):143–172.

51. Harley P, Fridd-Stroud V, Greenberg J, Guenther A, Vasconcellos P. Emission of 2-methyl-3-buten-2-ol by pines: A potentially large natural source of reactive carbon to the atmosphere. *J Geophys Res*. 1998;103(D19):25479–25486.
52. Goldan PD, Kuster WC, Fehsenfeld FC, Montzka SA. The observation of a C_5 alcohol emission in a North American pine forest. *Geophys Res Lett*. 1993;20(11):1039–1042.
53. Fisher AJ, Grimes HD, Fall R. The biochemical origin of pentenol emissions from wounded leaves. *Phytochemistry*. 2003;62(2):159–163.
54. Pfrang C, King MD, Braeckevelt M, Canosa-Mas CE, Wayne RP. Gas-phase rate coefficients for reactions of NO_3, OH, O_3 and $O(^3P)$ with unsaturated alcohols and ethers: Correlations and structure–activity relations (SARs). *Atmos Environ*. 2008;42:3018–3034.
55. McGillen MR, Archibald AT, Carey T, Leather KE, Shallcross DE, Wenger JC, Percival CJ. Structure–activity relationship (SAR) for the prediction of gas-phase ozonolysis rate coefficients: An extension towards heteroatomic unsaturated species. *Phys Chem Chem Phys*. 2011;13(7):2842–2849.
56. Long B, Bao JL, Truhlar DG. Atmospheric chemistry of Criegee intermediates: Unimolecular reactions and reactions with water. *J Am Chem Soc*. 2016;138(43):14409–14422.
57. Long B, Bao JL, Truhlar DG. Unimolecular reaction of acetone oxide and its reaction with water in the atmosphere. *Proc Natl Acad Sci USA*. 2018;115(24):6135–6140.
58. Newland MJ, Mouchel-Vallon C, Valorso R, Aumont B, Vereecken L, Jenkin ME, Rickard AR. Estimation of mechanistic parameters in the gas-phase reactions of ozone with alkenes for use in automated mechanism construction. *Atmos Chem Phys*. 2022;22(9):6167–6195.
59. Cremer D. Stereochemistry of the ozonolysis of alkenes: Ozonide- versus carbonyl oxide-control. *Angew Chem Int Ed*. 1981;20(10):888–889.
60. Cremer D. Theoretical determination of molecular structure and conformation. 8. Energetics of the ozonolysis reaction. Primary ozonide vs. carbonyl oxide control of stereochemistry. *J Am Chem Soc*. 1981;103(13):3627–3633.
61. Watson NA. An analysis of the sources and sinks for Criegee intermediates: An extended computational study [PhD thesis]. University of Cardiff; 2021. [accessed 15 Oct 2021] http://orca.cardiff.ac.uk/id/eprint/144742.
62. Vereecken L, Novelli A, Kiendler-Scharr A, Wahner A. Unimolecular and water reactions of oxygenated and unsaturated Criegee intermediates under atmospheric conditions. *Phys Chem Chem Phys*. 2022;24(11):6428–6443.
63. Long B, Bao JL, Truhlar DG. Kinetics of the strongly correlated $CH_3O + O_2$ reaction: The importance of quadruple excitations in atmospheric and combustion chemistry. *J Am Chem Soc*. 2019;141(1):611–617.
64. Galano A, Narciso-Lopez M, Francisco-Marquez M. Water complexes of important air pollutants: Geometries, complexation energies, concentrations, infrared spectra, and intrinsic reactivity. *J Phys Chem A*. 2010;114(10):5796–5809.
65. Brasseur G, Solomon S. *Aeronomy of the middle atmosphere: Chemistry and physics of the stratosphere and mesosphere*, 3rd edition ed.Germany: Springer; 2005.
66. Long B, Wang Y, Xia Y, He X, Bao JL, Truhlar DG. Atmospheric kinetics: Bimolecular reactions of carbonyl oxide by a triple-level strategy. *J Am Chem Soc*. 2021;143(22):8402–8413.
67. Lin L-C, Chang H-T, Chang C-H, Chao W, Smith MC, Chang CH, Jr-Min Lin J, Takahashi K. Competition between H_2O and $(H_2O)_2$ reactions with CH_2OO/CH_3CHOO. *Phys Chem Chem Phys*. 2016;18(6):4557–4568.
68. Anglada JM, Solé A. Impact of the water dimer on the atmospheric reactivity of carbonyl oxides. *Phys Chem Chem Phys*. 2016;18(26):17698–17712.
69. Vereecken L, Novelli A, Taraborrelli D. Unimolecular decay strongly limits the atmospheric impact of Criegee intermediates. *Phys Chem Chem Phys*. 2017;19(47):31599–31612.
70. Truhlar DG, Garrett BC. Variational transition-state theory. *Acc Chem Res*. 1980;13:440–448.
71. Bao JL, Truhlar DG. Variational transition state theory: Theoretical framework and recent developments. *Chem Soc Rev*. 2017;46(24):7548–7596.
72. Wigner E. The transition state method. *Trans Faraday Soc*. 1938;34:29–41.
73. Mahan BH. Activated complex theory of bimolecular reactions. *J Chem Educ*. 1974;51(11):709–711.
74. Tucker SC, Truhlar DG. Dynamical formulation of transition state theory: Variational Transition states and Semiclassical Tunneling. In: Betrán J, Czismadia IG, editors. *New theoretical concepts for understanding organic reactions*. Dordercht: Kluwer; 1989; 26: 291–346.
75. Gilbert RG, Smith SC. *Theory of unimolecular and recombination reactions*. Oxford: Blackwell; 1990. p. 33–39.
76. Klippenstein SJ. RRKM theory and its implementation. In: Green NJB, editor. *Comprehensive chemical kinetics*. Amsterdam: Elsevier; 2003. 39, p. 55–103.
77. Eyring H. The activated complex and the absolute rate of chemical reactions. *Chem Rev*. 1935;17(1):65–77.
78. Kreevoy MM, Truhlar DG. Transition state theory. In: Bernasconi CF, editor. *Investigation of rates and mechanisms of reactions, part I*. New York: Wiley; 1986. p. 13–95.
79. Pechukas P. Transition state theory. *Annu Rev Phys Chem*. 1981;32(1):159–177.
80. Anderson JB. Predicting rare events in molecular dynamics. *Adv Chem Phys*. 1995;91:381–431.
81. Field MJ. The simulation of chemical reactions. In: van Gunsteren WF, Weiner PK, Wilkinson AJ, editors. *Computer simulation of biomolecular systems*. Leiden: ESCOM; 1993. vol. 2. p. 82–123.
82. Yu T, Zheng J, Truhlar DG. Multi-structural variational transition state theory. Kinetics of the 1,4-hydrogen shift isomerization of the pentyl radical with torsional anharmonicity. *Chem Sci*. 2011;2(11):2199–2213.
83. Liu Y-P, Lynch GC, Truong TN, Lu D, Truhlar DG, Garrett BC. Molecular modeling of the kinetic isotope effect for the [1,5]-sigmatropic rearrangement of cis-1,3-pentadiene. *J Am Chem Soc*. 1993;115(6):2408–2415.
84. Bao JL, Truhlar DG. Silane-initiated nucleation in chemically active plasmas: Validation of density functionals, mechanisms, and pressure-dependent variational transition state calculations. *Phys Chem Chem Phys*. 2016;18(15):10097–10108.
85. Bao JL, Zheng J, Truhlar DG. Kinetics of hydrogen radical reactions with toluene including chemical activation theory employing system-specific quantum RRK theory calibrated by variational transition state theory. *J Am Chem Soc*. 2016;138(8):2690–2704.
86. Tan X-F, Zhang L, Long B. New mechanistic pathways for the formation of organosulfates catalyzed by ammonia and

carbinolamine formation catalyzed by sulfuric acid in the atmosphere. *Phys Chem Chem Phys*. 2020;22(16):8800–8807.
87. Long B, Xia Y, Truhlar DG. Quantitative kinetics of HO_2 reactions with aldehydes in the atmosphere: High-order dynamic correlation, anharmonicity, and falloff effects are all important. *J Am Chem Soc*. 2022;144(43):19910–19920.
88. Xia Y, Long B, Lin S, Teng C, Bao JL, Truhlar DG. Large pressure effects caused by internal rotation in the *s-cis-syn*-acrolein stabilized Criegee intermediate at tropospheric temperature and pressure. *J Am Chem Soc*. 2022;144(11):4828–4838.
89. Zhao Y-C, Long B, Francisco JS. Quantitative kinetics of the reaction between CH_2OO and H_2O_2 in the atmosphere. *J Phys Chem A*. 2022;126(38):6742–6750.
90. Zhang Y-Q, Xia Y, Long B. Quantitative kinetics for the atmospheric reactions of Criegee intermediates with acetonitrile. *Phys Chem Chem Phys*. 2022;24(40):24759–24766.
91. Long B, Bao JL, Truhlar DG. Rapid unimolecular reaction of stabilized Criegee intermediates and implications for atmospheric chemistry. *Nat Commun*. 2019;10:Article 2003.
92. Wang P-B, Truhlar DG, Xia Y, Long B. Temperature-dependent kinetics of the atmospheric reaction between CH_2OO and acetone. *Phys Chem Chem Phys*. 2022;24(21):13066–13073.
93. Xia Y, Long B, Liu A, Truhlar DG. Reactions with Criegee intermediates are the dominant gas-phase sink for formyl fluoride in the atmosphere. *Fundam Res*. 2023; DOI: 10.1016/j.fmre.2023.02.012.
94. Zheng J, Truhlar DG. Quantum thermochemistry: Multistructural method with torsional anharmonicity based on a coupled torsional potential. *J Chem Theory Comput*. 2013;9(3):1356–1367.
95. Garrett BC, Truhlar DG. Canonical unified statistical model. Classical mechanical theory and applications to collinear reactions. *J Chem Phys*. 1982;76(4):1853–1858.
96. Zhang L, Truhlar DG, Sun S. Association of Cl with C_2H_2 by unified variable-reaction-coordinate and reaction-path variational transition-state theory. *Proc Natl Acad Sci USA*. 2020;117(11):5610–5616.
97. Georgievskii Y, Klippenstein SJ. Variable reaction coordinate transition state theory: Analytic results and application to the $C_2H_3 + H \rightarrow C_2H_4$ reaction. *J Chem Phys*. 2003;118(12):5442–5455.
98. Zheng J, Zhang S, Truhlar DG. Density functional study of methyl radical association kinetics. *J Phys Chem A*. 2008;112(98):11509–11513.
99. Zheng J, Bao LJ, Meana-Pañeda R, Zhang S, Lynch BJ, Corchado JC, Chuang Y-Y, Fast PL, Hu W-P, Liu Y-P, Lynch GC, Nguyen KA, Jackels CF, Fernandez Ramos A, Ellingson BA, Melissas V, Villa J, Rossi I, Coitino L, Pu J, Albu TV, Steckler R, Garrett BC, Isaacson AD, Truhlar DG. *Polyrate* – version 2017-C; University of Minnesota, Minneapolis, 2018.
100. Georgievskii Y, Klippenstein SJ. MESS. [accessed 1 May 2019] https://tcg.cse.anl.gov/papr/codes/mess.html.
101. Zheng J, Mielke SL, Clarkson KL, Truhlar DG. *MSTor*: A program for calculating partition functions, free energies, enthalpies, entropies, and heat capacities of complex molecules including torsional anharmonicity. *Comput Phys Commun*. 2012;183(8):1803–1812.
102. Zheng J, Meana-Pañeda R, Truhlar DG. *MSTor* version 2013: A new version of the computer code for the multi-structural torsional anharmonicity, now with a coupled torsional potential. *Comput Phys Commun*. 2013;184(8):2032–2033.
103. Raghavachari K, Trucks GW, Pople JA, Head-Gordon M. A fifth-order perturbation comparison of electron correlation theories. *Chem Phys Lett*. 1989;157(6):479–483.
104. Knizia G, Adler TB, Werner H-J. Simplified CCSD(T)-F12 methods: Theory and benchmarks. *J Chem Phys*. 2009;130(5):Article 054104.
105. Martin JML, Kesharwani MK. Assessment of CCSD(T)-F12 approximations and basis sets for harmonic vibrational frequencies. *J Chem Theory Comput*. 2014;10(5):2085–2090.
106. Győrffy W, Werner H-J. Analytical energy gradients for explicitly correlated wave functions. II. Explicitly correlated coupled cluster singles and doubles with perturbative triples corrections: CCSD(T)-F12. *J Chem Phys*. 2018;148(11):Article 114104.
107. Bomble YJ, Stanton JF, Kállay M, Gauss J. Coupled-cluster methods including noniterative corrections for quadruple excitations. *J Chem Phys*. 2005;123(5):Article 054101.
108. Chan B, Radom L, . W2X and W3X-L: Cost-effective approximations to W2 and W4 with kj $mo1^{-1}$ accuracy. *J Chem Theory Comput*. 2015;11(5):2109–2119.
109. Wang Y, Verma P, Jin X, Truhlar DG, He X. Revised M06 density functional for main-group and transition-metal chemistry. *Proc Natl Acad Sci USA*. 2018;115(41):10257–10262.
110. Peterson KA, Adler TB, Werner H-J. Systematically convergent basis sets for explicitly correlated wavefunctions: The atoms H, He, B–Ne, and Al–Ar. *J Chem Phys*. 2008;128(8):Article 084102.
111. Parker TM, Burns LA, Parrish RM, Ryno AG, Sherrill CD. Levels of symmetry adapted perturbation theory (SAPT). I. Efficiency and performance for interaction energies. *J Chem Phys*. 2014;140(9):Article 094106.
112. Zhao Y, Truhlar DG. The M06 suite of density functionals for main group thermochemistry, thermochemical kinetics, noncovalent interactions, excited states, and transition elements: Two new functionals and systematic testing of four M06-class functionals and 12 other functionals. *Theor Chem Accounts*. 2008;120(9):215–241.
113. Alecu IM, Zheng J, Zhao Y, Truhlar DG. Computational thermochemistry: Scale factor databases and scale factors for vibrational frequencies obtained from electronic model chemistries. *J Chem Theory Comput*. 2010;6(9):2872–2887.
114. Zheng J, Meana-Pañeda R, Truhlar DG. Prediction of experimentally unavailable product branching ratios for biofuel combustion: The role of anharmonicity in the reaction of isobutanol with OH. *J Am Chem Soc*. 2014;136(13):5150–5160.
115. Bloino J, Biczysko M, Barone V. General perturbative approach for spectroscopy, thermodynamics, and kinetics: Methodological background and benchmark studies. *J Chem Theory Comput*. 2012;8(3):1015–1036.
116. Kuhler KM, Truhlar DG, Isaacson AD. General method for removing resonance singularities in quantum mechanical perturbation theory. *J Chem Phys*. 1996;104(12):4664–4671.
117. Werner H-J, Knowles PJ, Knizia G, Manby FR, Schütz M. Molpro: A general-purpose quantum chemistry program package. *WIREs Comput Mol Sci*. 2012;2(2):242–253.
118. Kállay M, Nagy PR, Mester D, Rolik Z, Samu G, Csontos J, Csóka J, Bernát Szabó P, Gyevi-Nagy L, Hégely B, et al.

The MRCC program system: Accurate quantum chemistry from water to proteins. *J Chem Phys*. 2020;152(7):Article 074107.

119. Frisch MJ, Trucks GW, Schlegel HB, Scuseria GE, Robb MA, Cheeseman JR, Scalmani G, Barone V, Petersson GA, Nakatsuji H, Li X, Caricato M, Marenich AV, Bloino J, Janesko BG, Gomperts R, Mennucci B, Hratchian HP, Ortiz JV, Izmaylov AF, Sonnenberg JL, Williams-Young D, Ding F, Lipparini F, Egidi F, Goings J, Peng B, Petrone A, Henderson T, Ranasinghe D, Zakrzewski VG, Gao J, Rega N, Zheng G, Liang W, Hada M, Ehara M, Toyota K, Fukuda R, Hasegawa J, Ishida M, Nakajima T, Honda Y, Kitao O, Nakai H, Vreven T, Throssell K, Montgomery JA Jr., Peralta JE, Ogliaro F, Bearpark MJ, Heyd JJ, Brothers EN, Kudin KN, Staroverov VN, Keith TA, Kobayashi R, Normand J, Raghavachari K, Rendell AP, Burant JC, Iyengar SS, Tomasi J, Cossi M, Millam JM, Klene M, Adamo C, Cammi R, Ochterski JW, Martin RL, Morokuma K, Farkas O, Foresman JB, Fox DJ, *Gaussian 16, Revision B.01*. Wallingford (CT): Gaussian Inc.; 2016.
120. Almatarneh MH, Elayan IA, Abu-Saleh AA-AA, Altarawneh M, Ariya PA. The gas-phase ozonolysis reaction of methylbutenol: A mechanistic study. *Int J Quantum Chem*. 2019;119(10):Article e25888.
121. Zhao Y, Truhlar DG. The M06 suite of density functionals for main group thermochemistry, thermochemical kinetics, noncovalent interactions, excited states, and transition elements: Two new functionals and systematic testing of four M06-class functionals and 12 other functionals. *Theor Chem Accounts*. 2008;120(1):215–241.
122. Zheng J, Truhlar DG. Multi-path variational transition state theory for chemical reaction rates of complex polyatomic species: Ethanol + OH reactions. *Faraday Discuss*. 2012;157:59–88.
123. Ruscic B. Active thermochemical tables: Water and water dimer. *J Phys Chem A*. 2013;117(46):11940–11953.